International Journal of Nanomedicine

Dovepress
open access to scientific and medical research

Open Access Full Text Article

ORIGINAL RESEARCH

Periodontal Ligament Stem Cell-Derived Small Extracellular Vesicles Embedded in Matrigel Enhance Bone Repair Through the Adenosine Receptor Signaling Pathway

Bingjiao Zhao[1,2], Qingqing Chen[2], Liru Zhao[3], Jiaqi Mao[3], Wei Huang[2], Xinxin Han[2], Yuehua Liu[1,2]

[1]Department of Orthodontics, Shanghai Stomatological Hospital, Fudan University, Shanghai, 200001, People's Republic of China; [2]Shanghai Key Laboratory of Craniomaxillofacial Development and Diseases, Fudan University, Shanghai, 200001, People's Republic of China; [3]Department of Orthodontics, School of Stomatology, Hebei Medical University, Shijiazhuang, 050017, People's Republic of China

Correspondence: Yuehua Liu, Department of Orthodontics, Shanghai Stomatological Hospital, Fudan University, 356 East Beijing Road, Shanghai, 200001, People's Republic of China, Tel +86-63298475, Fax +86-63614515, Email liuyuehua@fudan.edu.cn

Purpose: Small extracellular vesicles (sEVs) are natural biocarriers for biomolecule transfer between cells and promising therapeutic strategies for bone defect repair. In this study, human periodontal ligament stem cell (PDLSC)-derived sEVs (P-EVs) were immobilized in Matrigel to establish a topical cell-free transplantation strategy for bone repair.

Methods: PDLSCs were cultured and P-EVs were isolated from the culture supernatant. In a rat bilateral calvarial defect model, P-EV/Matrigel was plugged into one defect and PBS/Matrigel was applied to the other. Bone repair in vivo was assessed by micro-computed tomography, histomorphometry, and immunohistochemical staining. In vitro, we investigated the effects of P-EVs on the proliferation and migration capabilities of bone marrow mesenchymal stem cells (BMMSCs) and explored the potential mechanism of action.

Results: The in vivo study showed that P-EV/Matrigel accelerated bone tissue repair by increasing cell infiltration when compared with the control. In vitro, P-EVs enhanced proliferation and migration of BMMSCs via increased phosphorylation of AKT and extracellular signal-regulated kinase 1/2 (ERK1/2). The role of P-EV-induced adenosine receptor signaling in AKT and ERK1/2 phosphorylation was a key mediator during enhanced BMMSC migration.

Conclusion: These results are the first to demonstrate that P-EVs accelerated the repair of bone defects, partially through promoting cell proliferation and migration. P-EV/Matrigel, which combines topical EV-implantation and extracellular matrix scaffolds, provides a new cell-free strategy for bone tissue repair.

Keywords: small extracellular vesicles, periodontal ligament stem cells, osteogenesis, cell-free therapy, bone defects

Introduction

Reconstruction of large-sized bone defects remains a challenge. Mesenchymal stromal cell (MSC)-based therapy has shown promising results in bone regenerative medicine.[1,2] Similar to other cellular therapies, there are still considerable limitations restricting the wider clinical applications of MSCs, such as the operation and logistical problems in the accessibility, storage, and expansion of cells. Accumulating evidence has suggested that, rather than adopting long-term transplantation and differentiation, MSCs heal injured tissues by enhancing the activity of tissue-resident recipient cells via paracrine mechanisms.[2–4] MSCs exert many of their paracrine effects through the release of extracellular vesicles with the diameter of 50–1000 nm.[5] In particular, small extracellular vesicles (sEVs, 50–200 nm diameter) derived from MSCs transport transcription factors and genetic materials that play a role in cell communication and modulate the cellular activities of recipient cells.[6,7] Studies show that MSC-derived sEVs can facilitate calvarial and alveolar bone regeneration in diverse animal models.[8–10]

Received: 8 November 2021
Accepted: 11 January 2022
Published: 2 February 2022

Graphical Abstract

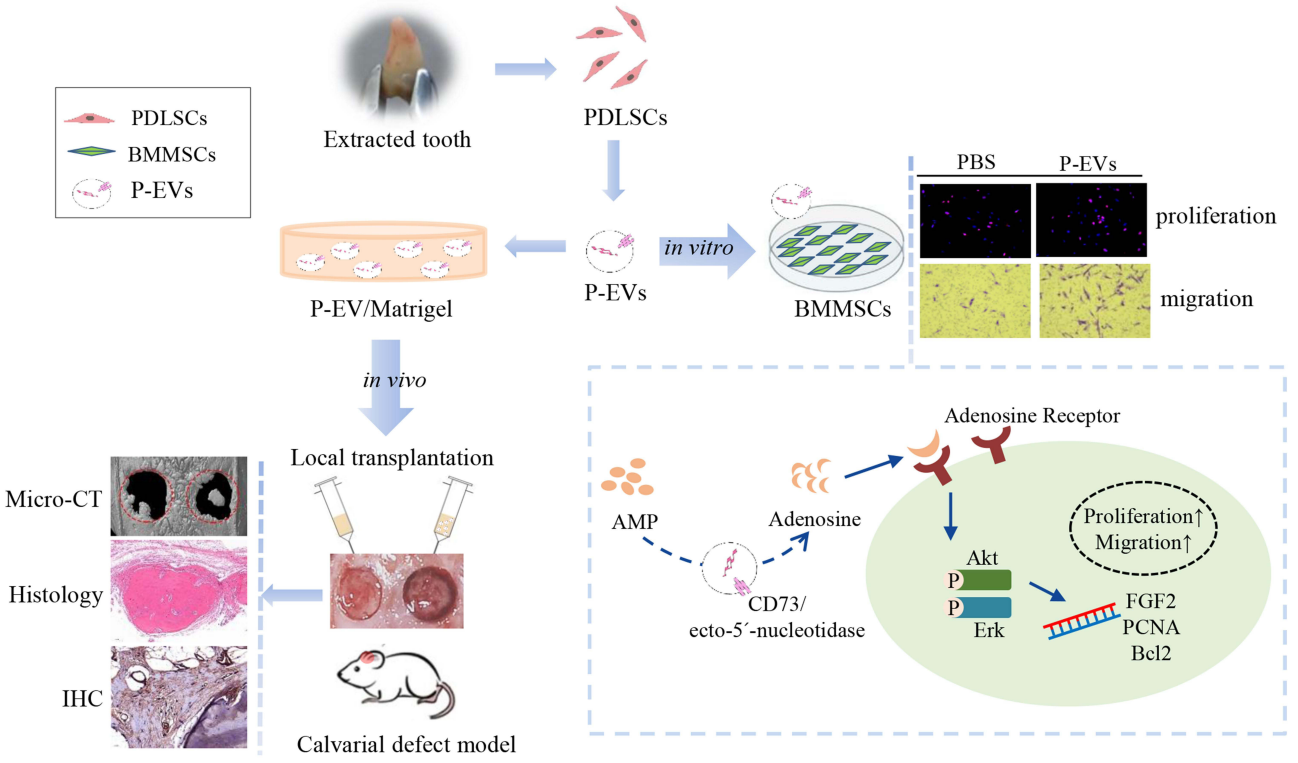

Human periodontal ligament stem cells (PDLSCs), which have a self-renewal capacity and potential for multi-lineage differentiation, are identified as MSCs residing in the periodontal ligament.[11,12] PDLSCs can be easily acquired from patients who require tooth extraction for orthodontic treatment or third molar extraction. PDLSC transplantation induces small molecular bioactive factors to surrounding cells and indirectly promotes bone regeneration.[4,13] Moreover, PDLSC conditioned medium promotes alveolar bone regeneration.[14] However, the effects of PDLSC-derived sEVs (P-EVs) on bone regeneration remain unknown.

For accelerating defect healing, efforts have been made to embed MSC-derived sEVs in hydrogels for site-specific delivery.[15,16] In the present study, P-EVs were isolated and their effects on bone tissue repair were investigated in a rat bilateral calvarial bone defect model. Corning Matrigel basement membrane was used as a scaffold for the local implantation of P-EVs in vivo. Matrigel has been widely used to carry cells and engineer three-dimensional (3D) environments to support cellular processes, such as cell proliferation, migration, and regeneration.[17,18] Moreover, because sEVs inherit the integrins present in the parent cell membrane, P-EVs were embedded in Matrigel to establish a local implantation strategy. Finally, to investigate the mechanism through which P-EVs participate in bone repair, the effects of P-EVs on the proliferation and migration of bone marrow mesenchymal stem cells (BMMSCs) were investigated in vitro. The results demonstrated that P-EVs embedded in Matrigel accelerated bone tissue repair via promoting surrounding host cell migration and proliferation, thereby providing insights into a new cell-free strategy for bone tissue repair based on topical sEV-implantation.

Materials and Methods

Cell Culture

Human PDLSCs were isolated from healthy premolars extracted for orthodontic treatment from three donors aged 11–13 years. The study complied with the Declaration of Helsinki and parents signed the informed consents for their children.

All procedures were approved by the Experiment and Ethics Committees of Shanghai Stomatological Hospital, Fudan University (NO. 20170007). Briefly, minced periodontal ligament tissues were incubated for 10 days, and PDLSCs were isolated from the primary periodontal ligament cells using the limiting dilution technique, as previously described.[19,20]

Human BMMSCs (ATCC PCS-500-012) were kindly provided by Dr. Xiao Zhang, Beijing University. BMMSCs were cultured in growth medium composed of alpha modified Minimum Essential Medium (αMEM; Gibco, Gaithersburg, MD, USA) supplemented with 15% fetal bovine serum (FBS; Gibco), 0.1 mM ascorbic acid (Sigma-Aldrich, St. Louis, MO, USA), 1% L-glutamine (Invitrogen, Carlsbad, CA, USA), and 1% antibiotic–antimycotic (Gibco). To induce osteogenic differentiation of BMMSCs, the cells were cultured in osteogenic medium composed of growth medium, 50 μg/mL ascorbic acid, 100 nM dexamethasone, and 10 mM β-glycerophosphate.

Isolation and Identification of P-EVs

PDLSCs (P5) were cultured in serum-free medium for 24 h, and P-EVs were isolated from the culture supernatant using the serial ultracentrifugation method.[8,10,21] Briefly, the supernatant was centrifuged at 300 × g for 5 min to pellet any contaminating cells, followed by centrifugation at 3000 × g for 15 min to eliminate cell debris. The resultant supernatant was filtered through a 0.22 μm filter to eliminate particles greater than 220 nm in size. The filtered supernatant was ultracentrifuged at 10,000 × g for 30 min and at 100,000 × g for 70 min at 4°C in an Optima XPN-100 Ultracentrifuge (Beckman Coulter, Fullerton, CA, USA). The obtained P-EV pellets were resuspended and pooled in 12mL PBS, followed by a second ultracentrifuged at 100,000 × g for 70 min. The purified P-EVs were resuspended in PBS and used for further examination.

Transmission electron microscopy (TEM) was performed to observe the morphology of P-EVs. The enriched P-EVs suspension (20 μL) was poured onto carbon-coated electron microscopic grids and air-dried for 5 min. The suspension was then incubated with a drop of 3% uranyl acetate for 5 min. The excess stain was removed. The images were captured using a Tecnai G2 Spirit TEM (FEI Company, Brno, Czech) at 100 kV.

The particle size distribution of P-EVs was measured using nanoparticle tracking analysis (NTA) with an NS300 nanoparticle analyzer (Nanosight, Malvern, Worcestershire, UK). The P-EVs were diluted in phosphate-buffered saline (PBS) (1:100), and three 30-s videos were recorded in different views using the script control function. Raw data were analyzed using analytical software (NTA version 2.3). Through Western blotting, the expression of sEV markers was determined, including CD63 (Santa Cruz, sc5275), CD9 (Santa Cruz, sc13118), CD81 (Santa Cruz, sc23962), TSG101 (Santa Cruz, sc7964), and glyceraldehyde 3-phosphate dehydrogenase (GADPH) (Santa Cruz, sc32233). In brief, PDLSCs and P-EVs were collected using lysis buffer, and equal amounts of proteins from each sample were extracted. Protein content was quantified using the Pierce BCA Protein Assay Kit (Thermo Fisher Scientific, Rockford, IL, USA) according to the manufacturer's protocol.

Cellular Uptake Assay

To investigate the kinetics of P-EVs uptake by BMMSCs, P-EVs were labeled with PKH26 using the PKH26 Red Fluorescent Cell Linker Kit (catalog number MIDI26, Sigma-Aldrich, Australia). First, 100 μg P-EVs were mixed with 250 μL of Diluent C (Part A), and 1 μL of the PKH26 dye solution was added to 250 μL of Diluent C to prepare the dye solution (Part B). Next, Part A was mixed with part B and incubated for 5 min before incubating with 500 μL of 1% bovine serum albumin (BSA) for 1 min to stop the reaction. PKH26-labeled P-EVs were washed with PBS and ultracentrifuged at 100,000 × g for 70 min at 4°C.

BMMSCs were seeded in glass-bottom cell culture dishes and incubated with PKH26-labeled P-EVs (10 μg/mL) for 1, 4, 24, 48, and 72 h at 37°C. The samples were washed three times with PBS and fixed with 4% paraformaldehyde. F-actin was stained with phalloidin (G1028, Servicebio, China), and the nuclei were stained with 6-diamidino-2-phenylindole solution (G1012, Servicebio, China). Images were captured using a confocal laser scanning microscope (TIR A1, Nikon, Tokyo, Japan).

Assessment of Proliferation of BMMSCs Cultured with P-EVs

BMMSCs were seeded onto a 96-well plate (5×10^3 cells per well) and incubated overnight. The cells were treated with P-EVs (0, 1, 5, and 10 μg/mL) in growth medium for 5 days. Cell viability was measured using a Cell Counting kit-8

(CCK-8; Dojindo, Kumamoto, Japan). The culture medium was discarded from each well, and 100 μL of 10% CCK-8 solution was added to each well. After incubation for 2 h, the absorbance values were measured at 450 nm using a multi-detection microplate reader (Epoch 2; Biotek, Winooski, VT, USA). Growth curves of BMMSCs cultured with P-EVs were plotted based on their optical densities (n = 5).

For cell proliferation assay, BMMSCs were seeded onto a 24-well plate (2×10^4 cells per well) and incubated overnight. The cells were incubated with 10 μM 5-bromo-2′-deoxyuridine (BrdU) and simultaneously exposed to P-EVs (0 and 10 μg/mL) for 12 h. BrdU incorporation was detected using a BrdU Immunohistochemistry Kit (#8850-6599, Invitrogen) according to the manufacturer's instructions. Images were captured using a fluorescence microscope (DMi8, Leica, Wetzlar, Germany), and the number of BrdU-incorporated cells was counted in five randomly selected fields per well.

Cell Migration Assay

Cell migration was evaluated using a non-contact transwell chamber with 8 μm pore filters (Corning, Kennebunk, ME, USA). Briefly, 5×10^3 BMMSCs were seeded onto the top well inserts, and 2.5 mL of medium containing P-EVs (0, 1, 5, and 10 μg/mL) was added to the lower compartment. After 24 h of culture, the chamber was washed three times with PBS. To eliminate non-migrated cells, the upper side of the top well inserts was gently wiped using cotton swabs. The top well inserts were fixed with 4% paraformaldehyde and stained with 0.5% crystal violet. Images were captured using a DMi8 microscope (Leica), and the number of migrated cells was counted in five randomly selected fields per well.

Scratch Assay

For the scratch assay, 5×10^4 BMMSCs per well were cultured in 12-well plates for 24 h to allow cell adhesion and reach 80% confluency. After the medium was changed to a low-serum (0.5% FBS) culture medium to reduce the rate of proliferation, the cell monolayer was mechanically "wounded" by scraping with a 200 μL sterile pipette tip. Cell monolayers were immediately washed with PBS, and images were captured. Cell monolayers were then treated with culture medium containing P-EVs (0, 1, 5, and 10 μg/mL). Images were captured at 0, 12, and 24 h after the scratch with the DM i8 Leica microscope. Cell migration rate was estimated as percent scratch closure using the ImageJ2× software (National Institutes of Health, Bethesda, MD, USA). All scratch assays were performed in triplicates, and three fields per well were analyzed.

Reverse Transcription Quantitative Polymerase Chain Reaction (RT-qPCR)

BMMSCs were seeded onto 6-well plates (2×10^5 cells/well) and incubated overnight. The cells were cultured with P-EVs (0, 1, 5, and 10 μg/mL) in growth medium for 2 days. Total RNA of BMMSCs was extracted with the TRIzol® reagent (Invitrogen) and quantified using NanoDrop2000 (Thermo Fisher Scientific), followed by cDNA synthesis. To evaluate the gene expression levels of osteogenic markers, RT-qPCR was performed in triplicates with the SYBR Green reagent (TaKaRa Bio Inc., Shiga, Japan) using a specified thermal cycler (LightCycler 96, Roche, USA). The proliferation-related marker genes whose expression levels were evaluated in the current study were proliferative cell nuclear antigen (PCNA), fibroblast growth factor 2 (FGF-2), and beclin 2 (BCL-2). The PCR program consisted of 40

Table 1 Primer Sequences for Quantitative RT-PCR

Gene Name	Primer Sequences Forward	Primer Sequences Reverse
FGF	AGAAGAGCGACCCTCACATCA	CGGTTAGCACACACTCCTTTG
PCNA	CCTGCTGGGATATTAGCTCCA	CAGCGGTAGGTGTCGAAGC
Bcl2	GGTGGGGTCATGTGTGTGG	CGGTTCAGGTACTCAGTCATCC
β-Actin	CATGTACGTTGCTATCCAGGC	CTCCTTAATGTCACGCACGAT

amplification cycles at 95°C for 10s, followed by 60°C for 30s. The primer sequences are listed in Table 1. Gene expression levels were calculated, and the values were normalized to that of the endogenous control β-actin.

Inhibition of Adenosine-Mediated AKT and Extracellular Signal-Regulated Kinase 1/2 (ERK1/2) Signaling

BMMSCs were seeded onto 6-well plates (2×10^5 cells/well) and cultured for 24 h. The cells were cultured in a low-serum culture medium for another 24 h, and the cells were treated with 10 μg/mL of P-EVs or PBS as the vehicle control. To study the phosphorylation of AKT and ERK1/2 and the role of adenosine receptor signaling, BMMSCs were pretreated with 10 μM MK2206 (AKT1/2/3 inhibitor, S1078, Selleck), 10 μM U0126 (ERK1/2 inhibitor, #9903, Cell Signaling Technology, Danvers, MA, USA), 1 mM theophylline (a non-selective adenosine receptor antagonist; M20489, Meryer, Shanghai, China) or an equivalent volume of dimethyl sulfoxide (DMSO) or distilled water as vehicle controls and incubated for 1 h prior to the treatment with P-EVs.

Western Blot Analysis

Western blotting was performed according to the standard protocols. Briefly, cells were collected using 2X lysis buffer containing a protease inhibitor cocktail. Proteins were separated on a 10% sodium dodecyl sulphate-polyacrylamide gel and then transferred onto a 0.45 μm polyvinylidene difluoride membrane. The membrane was blocked with 5% skimmed milk for 1h at room temperature and incubated with primary antibodies overnight at 4°C. The primary antibodies used were rabbit anti-Akt (1:1000, Cell Signaling Technology), anti-phospho-Akt (1:1000, Cell Signaling Technology), anti-Erk1/2 (1:1000, Cell Signaling Technology), anti-phospho-Erk1/2 (Thr202/Tyr204) (1:1000, Cell Signaling Technology), and mouse anti-GAPDH (1:500, Santa Cruz, sc32233). After washing the membranes three times in Tris-buffered saline and Tween 20 for 5 min, the membranes were incubated with the appropriate horseradish peroxidase-coupled secondary antibodies (1:10,000, Cell Signaling Technology) against the primary antibodies. Protein blots were visualized using an enhanced chemiluminescent substrate kit (ECL Advance; Thermo Fisher Scientific). The bands were visualized using an Amersham Imager 600 (GE Healthcare). Protein levels were calculated relative to that of GADPH, which was used as the control. Data were analyzed using the ImageJ software.

Incorporation of P-EVs into Matrigel

For local transplantation, P-EVs were immobilized on a Matrigel matrix basement membrane (354248, BD Biosciences, San Jose, CA), which was synthesized using a high concentration of Matrigel that acts as a carrier scaffold. For the experiment, P-EV/Matrigel was prepared using P-EVs (60 μg in 10 μL PBS) mixed with 10 μL Matrigel matrix solution on ice. The control group (PBS/Matrigel) was prepared using 10 μL PBS mixed with 10 μL Matrigel matrix solution. After being placed at 37°C for 30 min, the Matrigel samples formed a self-supporting gel scaffold.

To observe the surface morphology, scanning electron microscopy (SEM) was performed with gold sputter coating of freezing-dried Matrigel samples and imaging with a scanning electron microscope (s-4800, Hitachi, Japan) operating at 1.0 kV. To evaluate the distribution of P-EVs in Matrigel, the P-EVs were labeled with PKH26, and the construction of the P-EV/Matrigel was captured using a confocal laser-scanning microscope.

Transplantation of P-EV/Matrigel in a Rat Bilateral Critical-Sized Calvarial Defect Model

All study protocols were reviewed and approved by the Experiment and Ethics Committee of Shanghai Stomatological Hospital, Fudan University (20170007). All procedures were performed according to the Guide for the Care and Use of Laboratory Animals. Eight-week-old male Sprague–Dawley rats were maintained in a specific-pathogen-free environment with a 12 h light/dark cycle and free access to water and food. Bilateral calvarial defects were created as previously described.[18] Briefly, rats were anesthetized through an intraperitoneal injection of 2% pentobarbital sodium (0.3 mL/100 g body weight). Under low-speed drilling, two defects (5 mm in diameter) were made at the calvaria using a trephine bur. Saline irrigation was used to avoid heat-induced osteonecrosis, and a gentle operation was needed to avoid damage to the

dura mater and brain. The two critical-sized calvarial defects were then randomly assigned to the P-EV/Matrigel and control groups (n=10). In the same animal, 20 μL P-EV/Matrigel was plugged into one defect, and PBS/Matrigel was applied to the other. The incision was then sutured with 4–0 Vicryl sutures, and all animals received 80,000 units of penicillin through intramuscular injection.

Microcomputed Tomography (Micro-CT) Analysis

At 10 weeks after transplantation, the rats were euthanized via CO_2 inhalation, and all specimens were harvested. The calvariae were fixed in 4% paraformaldehyde. To visualize the healing of the skull defects, a conical beam micro-CT scanner (40 kV voltage, 250 μA current, 0.24 s integration time, Sky-Scan 1076; Bruker micro-CT, Kontich, Belgium) was used for scanning with an isotropic voxel size of 18 μm thickness. The 3D images were reconstructed from the scan data using the NRecon v.1.6.9 software. To evaluate bone tissue formation, the percentages of new bone volume relative to tissue volume (BV/TV) and bone mineral density (BMD) in the defects were estimated.

Histological and Immunohistochemistry Analysis

After micro-CT imaging, the whole calvaria was decalcified for 4 w in 10% ethylenediaminetetraacetic acid (pH 7.4). Following decalcification, the specimen was dehydrated with graded ethanol, embedded in paraffin, and sectioned at a thickness of 5 μm. The sections were stained with hematoxylin–eosin (HE) and Masson's trichrome stains. The stained sections were scanned using a digital slide scanner (Pannoramic DESK, P-MIDI, P250, 3D HISTECH, Hungary). The images were captured using a Pannoramic Scanner and visualized with the CaseViewer 2.3 software.

For immunohistochemical analysis of tissues, the sections were deparaffinized and rehydrated before being treated for antigen retrieval with boiled 10 mM citrate buffer for 10 min. Non-specific protein binding was blocked through incubation with 5% BSA solution at room temperature for 30 min. Primary antibodies against PCNA (1:400, ab92552, Abcam) were applied overnight at 4°C. After washing with PBS three times, the slides were incubated with secondary antibodies (1:1000, Abcam, UK) at room temperature for 1 h. The slides were stained with 3,3′-diaminobenzidine (Boster, Wuhan, China) chromogen and incubated for 5 min at room temperature to visualize the antibody-antigen reaction. The stained sections were dehydrated and covered using a coverslip before capturing the images using a Pannoramic digital slide scanner. For quantification of PCNA, a region of interest (ROI) of approximately 0.1 mm2 was defined, and positively stained cells were counted at 200 × magnification and expressed as a percentage of positively stained cells present in the ROI.

Statistical Analysis

All data are presented as mean ± standard deviation. Statistical analysis was performed via one-way analysis of variance using the SPSS software (version 20.0). Statistical analysis of in vivo calvarial defects were performed using pairwise one-tailed Student's *t*-tests. For in vitro assay, statistical analysis between two groups was performed by independent two-tailed Student's *t*-tests. Among multiple groups, statistical analyses were performed using the Tukey-Kramer Multiple Comparisons Test with one-way analysis of variance (ANOVA). P values < 0.05 were considered statistically significant. Figures were prepared using the GraphPad software (version 6.0; GraphPad Software, Inc., USA).

Results

Characterization of sEVs Derived from PDLSCs

The vesicles derived from PDLSCs were isolated successfully using a standard ultracentrifugation protocol. TEM images of the vesicles indicated double-membrane structures and cup-shaped morphologies (Figure 1A). To confirm the size distribution of the isolated vesicles, NTA was performed, and the results showed a mean particle size of 113.5 ± 32.25 nm and an approximate concentration of $4.5 + 1.3\times10^{11}$ particles/mL (Figure 1B). Extensive biochemical profiling of P-EVs was performed through Western blot analysis (Figure 1C). The results showed that these particles expressed the protein encoded by the tumor susceptibility gene 101, which is involved in multivesicular body biogenesis, and the characteristic

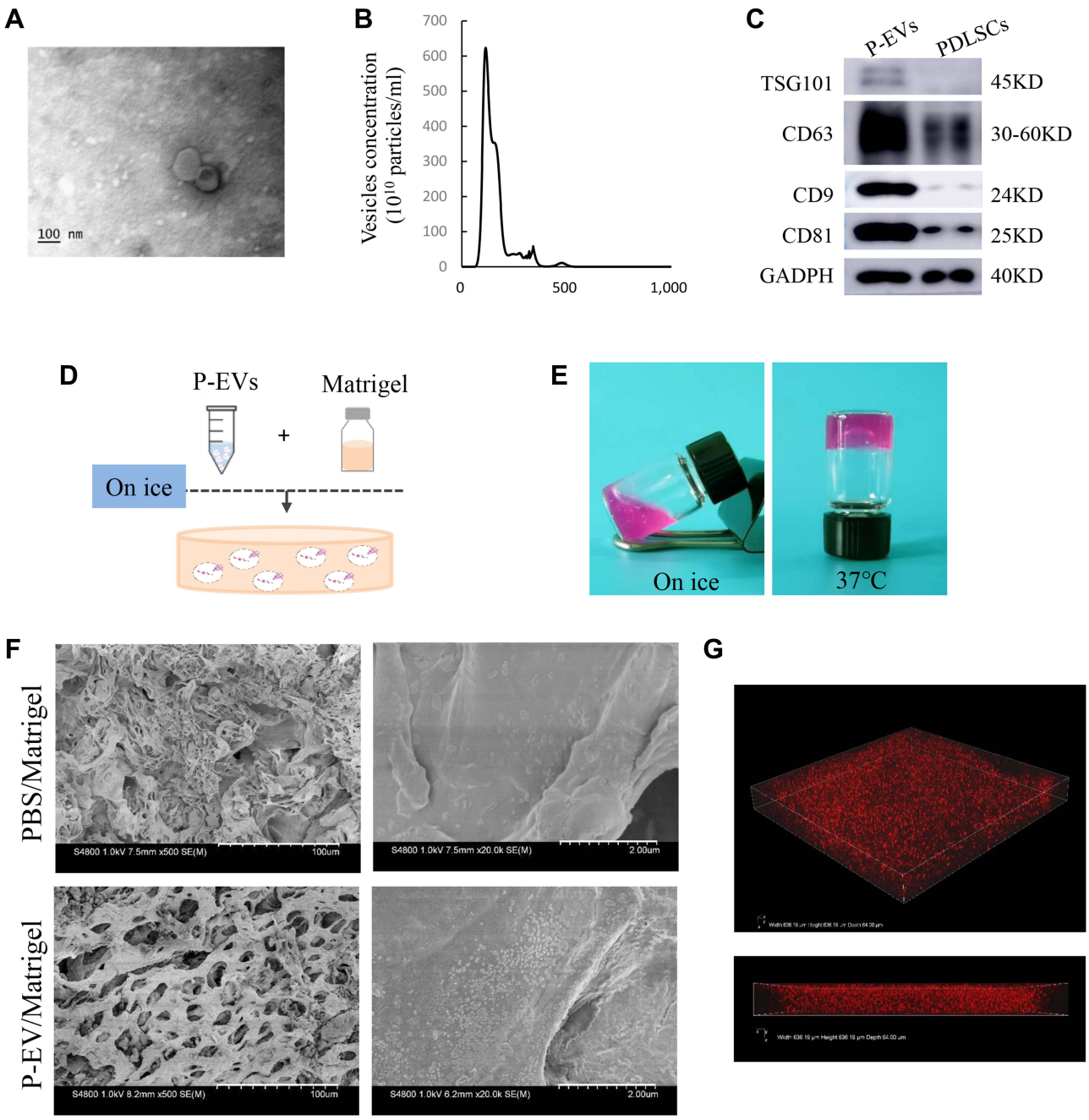

Figure 1 Characterization of human periodontal ligament stem cell-derived small extracellular vesicles (P-EVs) and delivery by Matrigel. (**A**) Morphology of P-EVs observed via transmission electron microscopy (TEM). Scale bar = 100 nm. (**B**) Particle size distribution of P-EVs measured by nanoparticle tracking analysis (NTA): mean size ± standard deviation of P-EVs was 113.5 ± 32.25 nm. (**C**) Western blot analysis of P-EV surface markers. (**D**) Preparation of the mixture of P-EVs and Matrigel on ice. (**E**) Gross appearance of P-EV/Matrigel on ice and at 37°C. (**F**) Scanning electron microscopy (SEM) image of P-EV/Matrigel and PBS/Matrigel. Scale bar = 100 μm (left) and 2 μm (right). (**G**) Confocal laser microscopy images of P-EV/Matrigel are shown in angled three-dimensional and z-stack views (Width 636.19μm, Height 636.19μm, Depth 64μm).

sEV tetraspanins such as CD9, CD63, and CD81. Taken together, the characterization based on morphology, size, and protein markers indicated that the vesicles were predominantly sEVs.

Preparation and Properties of the P-EV/Matrigel

For local transplantation of P-EVs, P-EV/Matrigel was prepared by mixing P-EVs with Matrigel matrix solution on ice (Figure 1D). As shown in Figure 1E, the P-EV/Matrigel changed from a dispersed matrix solution on ice to a stable gel

scaffold at 37 °C, which is shown by the tube inversion method. These results are consistent with the information provided by the manufacturer that a rapid gel process at >10 °C is typical for Matrigel solution.

SEM analysis showed that the freeze-dried Matrigel scaffolds had interconnected pores and sEVs distributed on the surface of P-EV/Matrigel, whereas no sEVs were observed on the control (Figure 1F). P-EVs were labeled with PKH26 and encapsulated in Matrigel. Confocal laser microscopy images revealed a 3D spatial distribution of labeled P-EVs in Matrigel (Figure 1G).

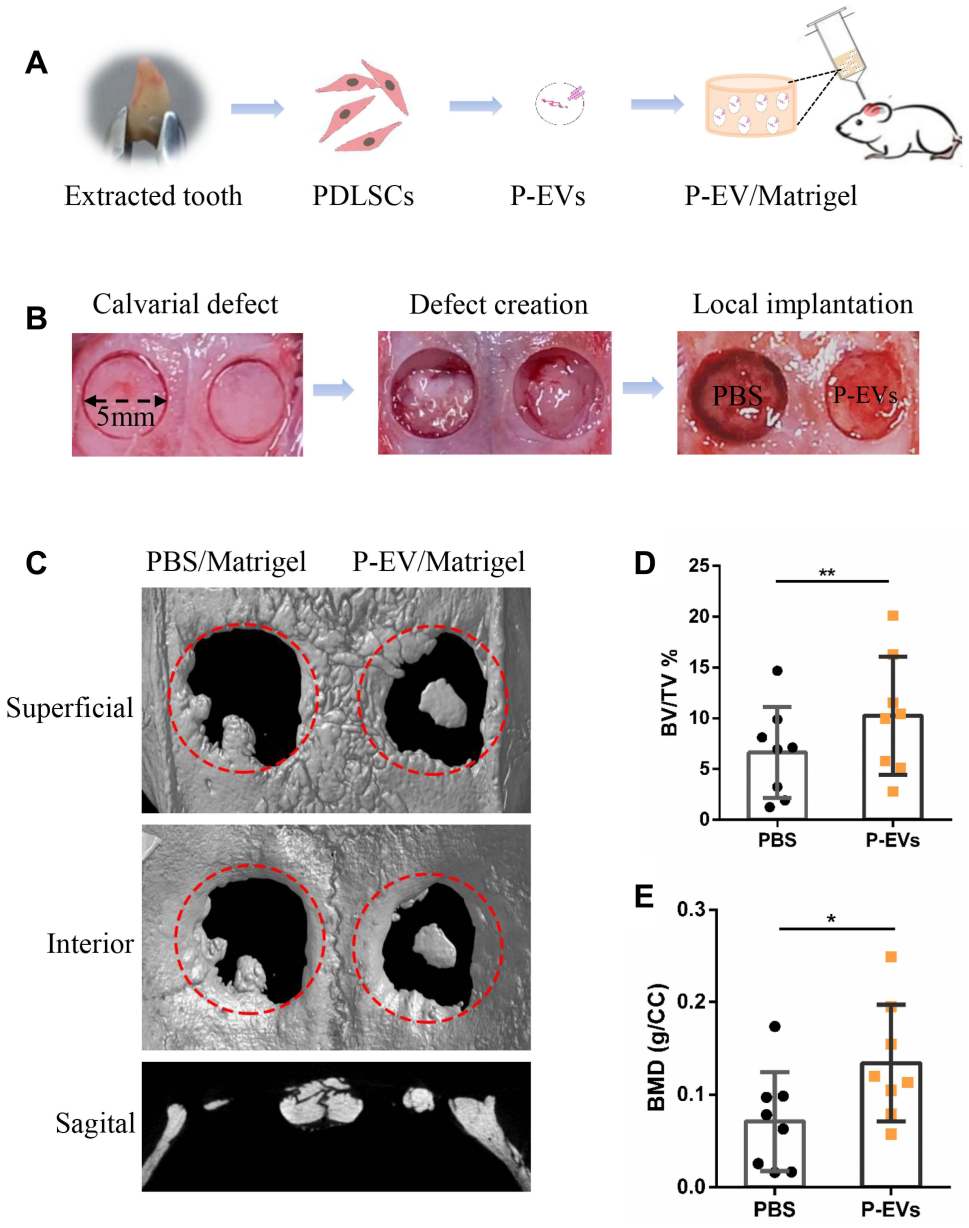

Figure 2 Formation of a bilateral critical-sized calvarial defect model and local transplantation of periodontal ligament stem cell-derived small extracellular vesicles (P-EVs). (**A**) Diagram of isolation and local transplantation of P-EVs. (**B**) In both sides of the calvaria, full-thickness bone defects (diameter = 5 mm) were created using a trephine drill. Either of the calvarial defects was filled with P-EVs immobilized in Matrigel (P-EV/Matrigel) randomly, and the other was filled with Matrigel incorporated with phosphate-buffered saline (PBS) (PBS/Matrigel) as the control. (**C**) Representative three-dimensional reconstruction and sagittal images of calvarial defects at 10 weeks posttransplantation. (**D**) Bone volume/tissue volume (BV/TV) and (**E**) bone mineral density (BMD) of the control and P-EVs group. P-EV/Matrigel increased bone repair in rat critical-sized calvarial defects. *$P < 0.05$, **$P < 0.01$.

P-EVs Immobilized in Matrigel Enhanced Bone Repair in vivo

sEVs derived from PDLSCs and immobilized in Matrigel were transplanted locally to rat calvarial defects (Figure 2A). Full-thickness bone defects were created on both sides of the calvaria, P-EV/Matrigel was applied on either side, and PBS/Matrigel was applied on the other side as an autogenous control (Figure 2B). To evaluate the therapeutic potential of P-EVs in bone repair, high-resolution micro-CT scanning of the bilateral calvarial defects was performed after 10 weeks (Figure 2C). Quantitative analysis of BV/TV showed a significant increase in bone repair with the local implantation of P-EVs when compared with the control side ($P = 0.008$, Figure 2D). Similar results were obtained in the case of local BMDs, which were increased significantly in the P-EV-treated side ($P = 0.01$, Figure 2E), indicating that P-EVs could enhance ossification in the bone defect.

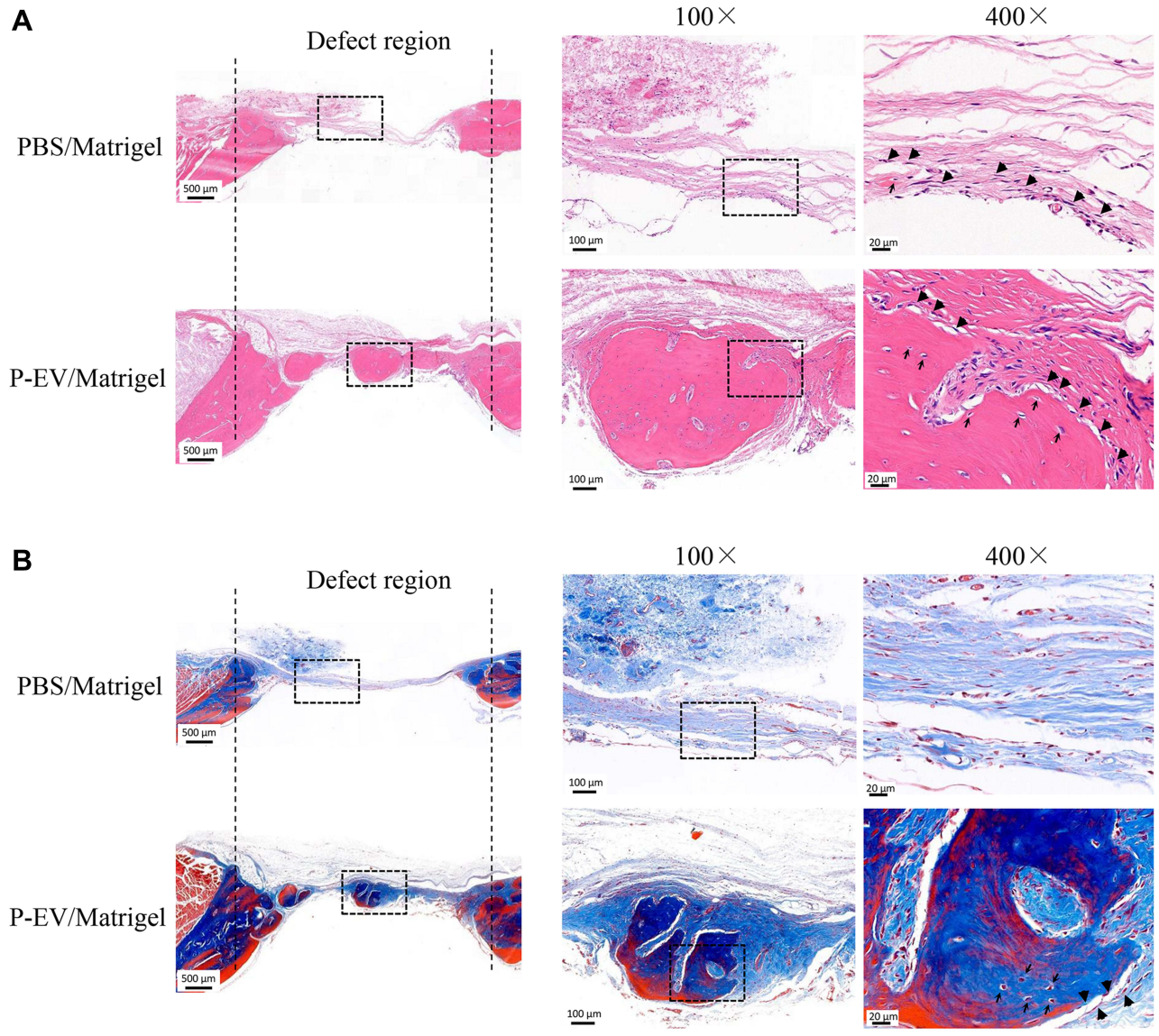

Figure 3 Histological analysis of bone repair on both sides of the bilateral calvarial bone defects in a rat model. (**A**) Formation of new bone-like tissue was confirmed histologically in the hematoxylin and eosin-stained defects on both sides. Few undegraded gels were observed, and bone repair was achieved on both sides. On the control side, Matrigel transplantation induced minimal osteoid formation (black big arrow) in the defect area. On the P-EV/Matrigel side, evident deposition of osteoid was observed, and osteoid calcification leading to bone formation was observed in the middle of the defect area. Embedded osteocyte-like cells (thin arrow) in the calcified osteoid were observed. (**B**) Corresponding Masson's trichrome staining. On the control side, the margins of the defects were connected via a thin dense connective fibrous tissue. On the P-EV/Matrigel side, the defect was occupied by dense fibrous connective tissue with bone-like tissue. On the P-EV/Matrigel side, osteocyte-like cells (thin arrow) were embedded in the newly immature bone tissue. PBS, phosphate-buffered saline; P-EV, periodontal ligament stem cell-derived small extracellular vesicle. Scale bar =500 μm (in 20× images), 100 μm (in 100× images) and 20 μm (in 400× images).

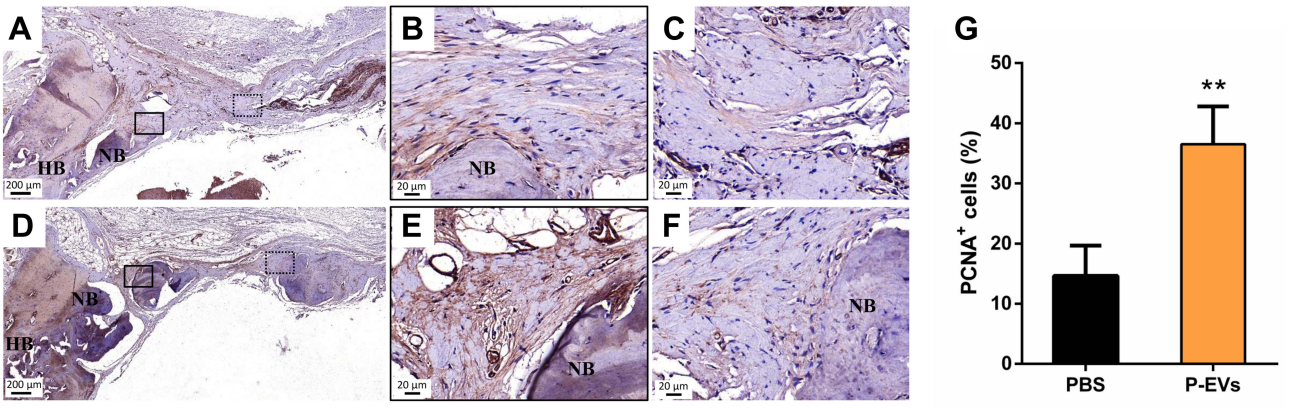

Figure 4 Evaluation of cell proliferation in the bone repair area. (**A**–**C**) Immunohistochemical staining of proliferative cell nuclear antigen (PCNA) in the control side. (**D**–**F**) More PCNA+ cells were found in the side treated with periodontal ligament stem cell-derived small extracellular vesicles (P-EVs). Black boxes indicate the region near the host bone, and the dotted boxes indicate the region in the middle of the defect. (**A** and **D**) scale bar = 200 μm (in); (**B** and **C, E** and **F**) scale bar = 20 μm. (**G**) Quantitative analysis of PCNA+ cells on both sides of the bilateral calvarial bone defects in a rat model. PCNA+ cells were counted under 200× magnification and expressed as the percentage of positively stained cells. Data are expressed as mean ± standard deviation (representative images, n = 5). $^{**}P < 0.01$.
Abbreviations: PBS, phosphate-buffered saline; P-EV, periodontal ligament stem cell-derived small extracellular vesicle.

At 10 weeks postoperatively, histological assessments of the bilateral calvarial defects were performed at various levels of magnification. Compared to the control side in the same HE-stained section, increased callus formation within the defect areas was observed in the P-EV/Matrigel side (Figure 3A). With local P-EVs treatment, deposition of the osteoid was observed, and osteoid calcification led to the formation of new bone tissues. On the control side, minimal osteoid tissue formation was observed around the margins of the defects. In Masson's trichrome-stained sections (Figure 3B), we observed that the defect was occupied by dense connective tissues with new bone-like tissues present on the P-EV/Matrigel-treated side. The red-stained mature bone was observed along the margin of the defect and osteocyte-like cells were embedded in the newly immature bone tissue. While, on the control side, the margins of the defect were connected by loose connective fibrous and thin bone-like tissues, with few undegraded gels.

To evaluate cell proliferation in the bone repair process, immunohistochemical staining of $PCNA^+$ cells was performed within the defect areas (Figure 4A–F). The P-EV/Matrigel-treated side showed a significant increase in the percentage of proliferating PCNA+ cells (36.49 ± 6.29%) compared with the control side (14.6 ± 25.03%, $P = 0.009$) (Figure 4G).

Uptake of P-EVs

To assess the kinetics of P-EV uptake by BMMSCs, BMMSCs were co-cultured with PKH26-fluorescent labeled P-EVs for 72 h. Confocal microscopy images revealed that the uptake of P-EVs by BMMSCs was rapid, and the cells became fluorescent after 1 h. PKH26-labeled P-EVs (in red) were gradually internalized into the cytoplasm of BMMSCs within 1–4 h of the treatment (Figure 5A). At 24 h, a large number of P-EVs were internalized, and maximum fluorescence intensity was achieved. Moreover, PKH26-labeled P-EVs were initially visible after 1 h in the cell membrane region when visualized under high magnification (Figure 5B). After 4 h, more P-EVs were internalized and were distributed in the perinuclear region of the cytoplasm. After 24 h, the intensity of red fluorescence began to decrease, which could be attributed to the metabolism of BMMSCs. These observations were consistent with the fluorescence analysis results, suggesting that the process of P-EV uptake by BMMSCs is time-dependent and saturable.

Effects of P-EVs on BMMSC Migration and Proliferation

The effects of P-EVs on the growth of BMMSCs were evaluated using the CCK-8 assay. During the 5-day monitoring period, BMMSC proliferation increased with time (Figure 6A). At day 1, 5 μg/mL P-EV treatment significantly enhanced the growth of BMMSCs ($P < 0.01$) compared to PBS treatment. Moreover, from day 3 onwards, cell growth increased significantly ($P < 0.01$) with P-EV treatment in a dose-dependent manner. After 5 days, BMMSCs treated with 10 μg/mL

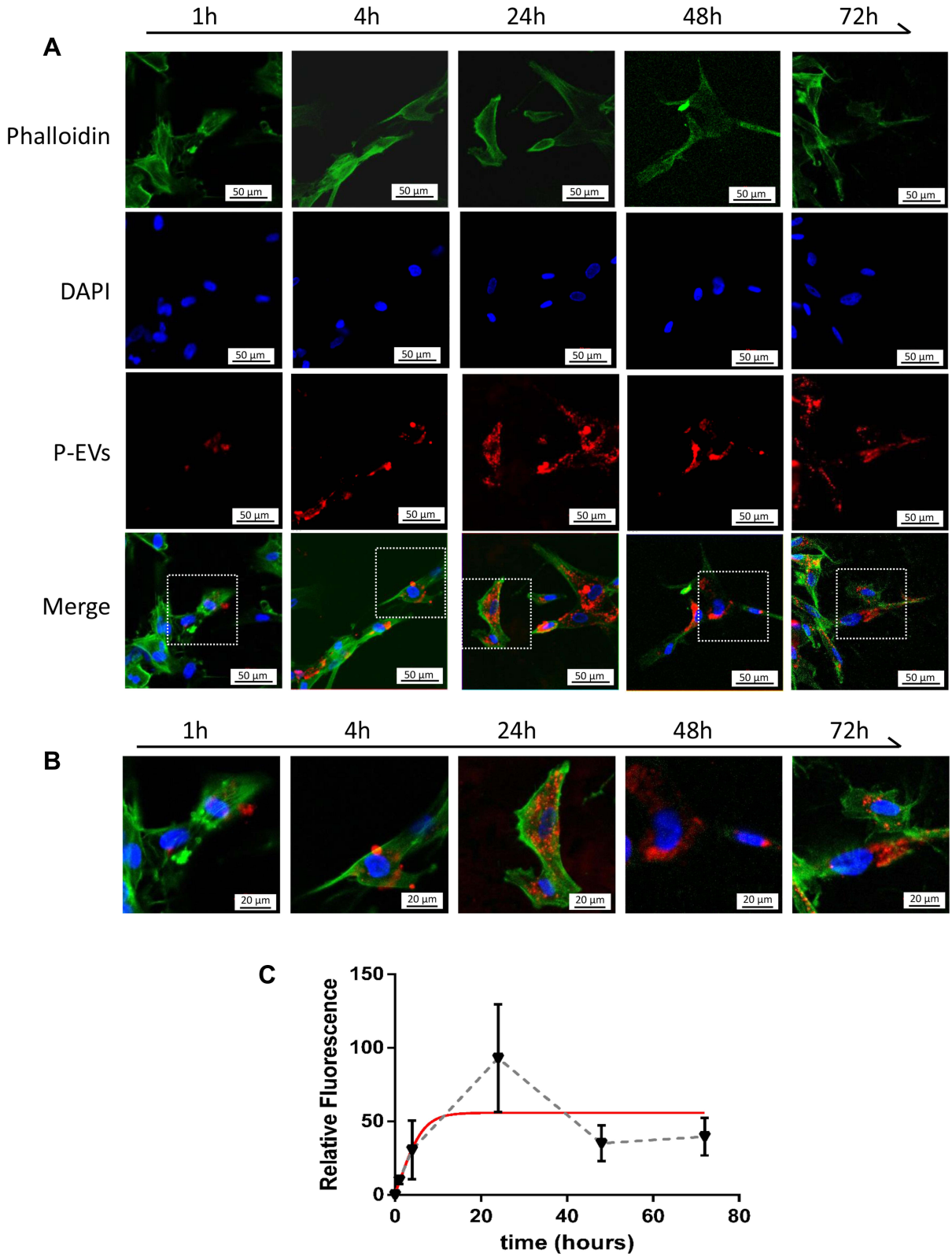

Figure 5 Cellular uptake assay of periodontal ligament stem cell-derived small extracellular vesicles (P-EVs) by bone marrow mesenchymal stem cells (BMMSCs). (**A**) BMMSCs were incubated with PKH26-labeled P-EVs (red) for 1, 4, 24, 48 and 72 h at 37 °C. Confocal microscopy images demonstrated rapid uptake of P-EVs. The cells were stained for F-actin (green) and nucleus (blue). Scale bar = 50 μm (**B**) Merged images at high magnification revealed cytoplasmic localization of P-EVs. Scale bar = 20 μm. (**C**) Graph showing the gradual internalization of P-EVs by BMMSCs within 72 h. The red line indicates a fitting curve to the data with nonlinear regression, suggesting saturable P-EV endocytosis. Relative fluorescence intensity was expressed as mean ± standard deviation (n = 5).
Abbreviation: DAPI, 4′,6-diamidino-2-phenylindole.

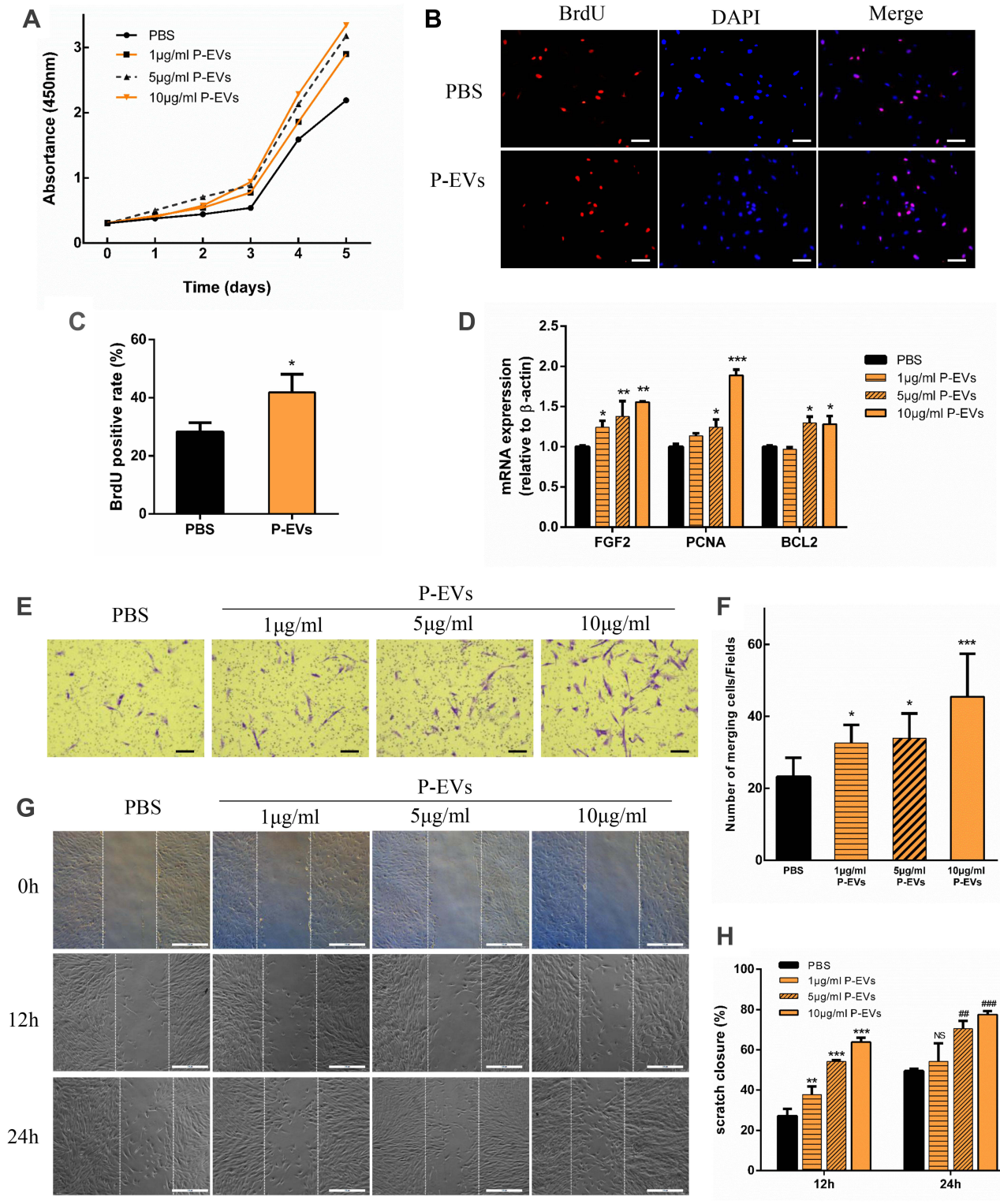

Figure 6 Effects of periodontal ligament stem cell-derived small extracellular vesicles (P-EVs) on bone marrow mesenchymal stem cell (BMMSC) proliferation and migration. (**A**) Growth curves of BMMSCs were measured using a cell counting kit-8 (CCK-8) assay kit. (**B**) Representative images of 5-bromo-2′-deoxyuridine (BrdU) assay. Scale bar = 100 μm. (**C**) BrdU assay showed a significant effect of P-EVs on BMMSC proliferation. *$P < 0.05$. (**D**) Quantitative RT-PCR analysis of genes associated with cell survival and proliferation. (**E** and **F**) P-EV treatment significantly enhanced cell migration when compared with vehicle treatment, in a dose-dependent manner. Migration rates of P-EV-treated BMMSCs were significantly higher than those of vehicle-treated cells. (**E**) scale bar = 100 μm. (**G** and **H**) Representative photomicrograph of the wound edge during the scratch assay at 0, 12 and 24 h after the treatment with P-EVs and vehicle. The migration rate of BMMSCs is represented as percent scratch closure. (**G**) scale bar = 200 μm. Each bar represents mean ± standard deviation values from three independent experiments. *$P < 0.05$, **$P < 0.01$, and ***$P < 0.001$ compared to PBS treatment at 12h. $^{\#\#}P < 0.01$ and $^{\#\#\#}P < 0.001$ compared to PBS treatment at 24h. Pairwise one-tailed Student's t-tests were used for statistical analysis.

Abbreviations: PBS, phosphate-buffered saline; DAPI, 4′,6-diamidino-2-phenylindole.

P-EVs showed a 1.53-fold higher proliferation rate than the control group. Consistent with the results of cell growth, BrdU incorporation assay results showed that P-EV treatment induced the proliferation of BMMSCs as early as 12 h (Figure 6B). The percentage of BrdU-positive cells in the P-EV-treated group (41.86 ± 6.25%) was significantly higher than that in the control group (28.27 ± 3.14%, $P = 0.03$) (Figure 6C). Similarly, after 2 days of P-EV treatment, mRNA expression of genes associated with cell survival and proliferation (PCNA, FGF-2, and BCL-2) was significantly upregulated when compared with the control group (Figure 6D).

Transwell migration assay results showed that the number of BMMSCs migrating through the membrane was significantly increased by P-EV treatment in a dose-dependent manner when compared with the PBS control (Figure 6E and F). A 1.98-fold increase in cell migration was observed in the 10 μg/mL P-EV-treated group ($P < 0.001$). To further study P-EV-induced cell migration during the process of bone repair, a scratch assay was performed in vitro to monitor wound healing.[22,23] Compared with the vehicle control, the migration rate of BMMSCs was significantly enhanced by P-EV treatment in a time- and dose-dependent manner (Figure 6G). Overall, 2.35- ($P < 0.001$) and 1.57-fold ($P < 0.001$) higher migration rates at 12 and 24 h, respectively, were observed in the 10 μg/mL P-EV-treated group than in the control group (Figure 6H). Thus, the results indicate that P-EVs have the potential to rapidly enhance the cell migration of BMMSCs.

P-EVs Enhance BMMSC Migration via Adenosine Receptor-Mediated AKT and ERK1/2 Signaling

As the AKT and ERK1/2 signaling pathways play a crucial role in P-EV-induced cell survival, the effect of P-EVs treatment on AKT and ERK1/2 phosphorylation in BMMSCS was examined.[8,19] P-EVs treatment significantly enhanced AKT and ERK1/2 phosphorylation within 15 min ($P < 0.01$, and $P < 0.05$, respectively; Figure 7A–C). P-EV-induced AKT phosphorylation was

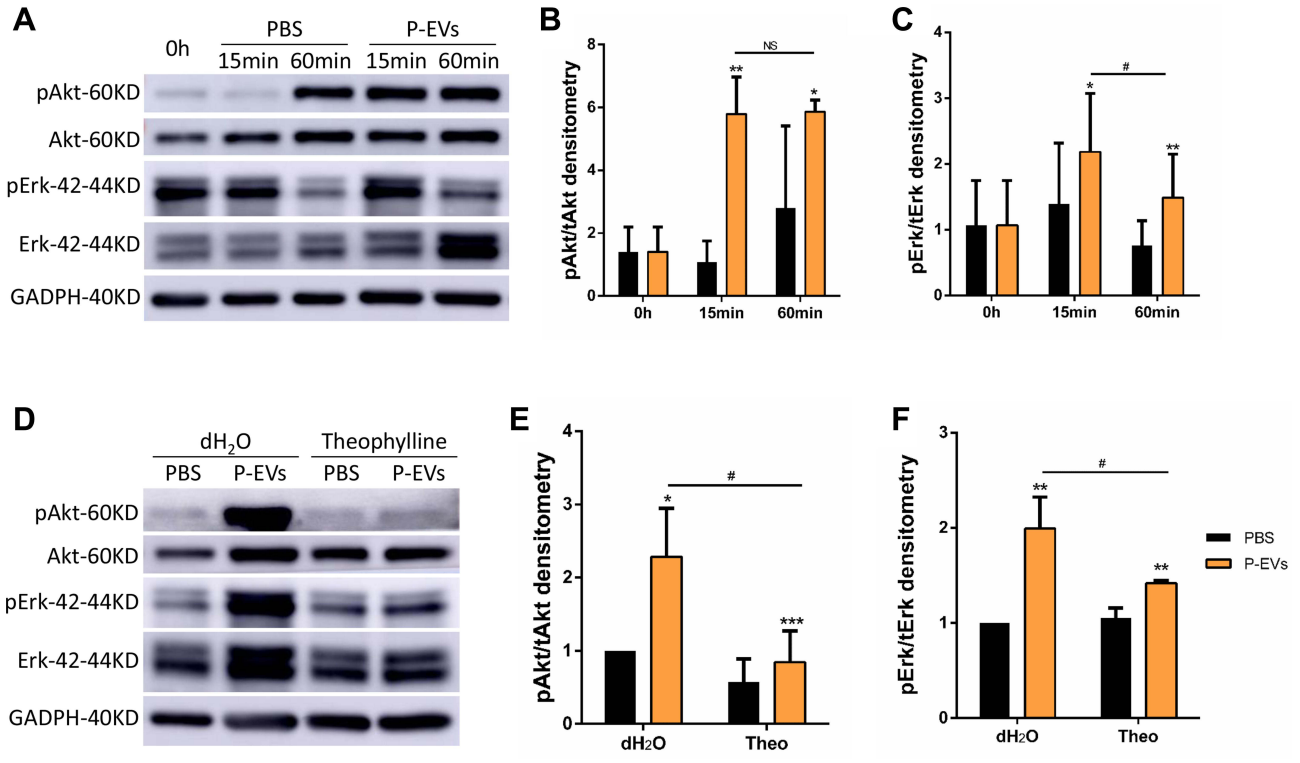

Figure 7 Periodontal ligament stem cell-derived small extracellular vesicle (P-EV) mediated partial activation of Akt and Erk1/2 phosphorylation through adenosine signaling. (**A**–**C**) After P-EV treatment, intracellular signaling in BMMSCs showed rapid activation of the Akt and Erk1/2 signaling pathways. *$P < 0.05$ compared to phosphate-buffered saline (PBS) treatment, **$P < 0.01$ compared to PBS treatment, $^{\#}P < 0.05$ compared to P-EV treatment after 60 min. (**D**–**F**) Western blot analysis revealed that pretreatment with theophylline (1 mM), a non-selective adenosine receptor antagonist, attenuated Akt phosphorylation by 2.7 folds and Erk1/2 phosphorylation by 1.4 folds. *$P < 0.05$, **$P < 0.01$, and***$P < 0.001$ compared to PBS treatment, $^{\#}P < 0.05$ compared to theophylline + P-EV treatment. Representative results from three independent experiments are expressed as mean ± standard deviation.

persistently elevated for up to 60 min ($P > 0.05$), whereas ERK1/2 phosphorylation peaked at 15 min and declined at 60 min ($P < 0.05$). These results indicate that P-EVs can rapidly activate the cellular metabolic activity of BMMSCs.

Next, we investigated whether adenosine receptors are the upstream mediators of P-EV-induced AKT and ERK1/2 phosphorylation because MSC-derived sEVs may convert extracellular adenosine monophosphate (AMP) to adenosine and elicit AKT and ERK1/2 signaling via adenosine receptor. After pretreatment with the non-selective adenosine receptor antagonist theophylline, P-EV-mediated phosphorylation of AKT in BMMSCs was significantly reduced ($P < 0.05$), and the extent of ERK1/2 phosphorylation was attenuated ($P < 0.05$) (Figure 7D–F). However, compared with the PBS control, P-EV-mediated AKT and ERK1/2 phosphorylation was not completely abrogated by theophylline treatment ($P < 0.001$ and

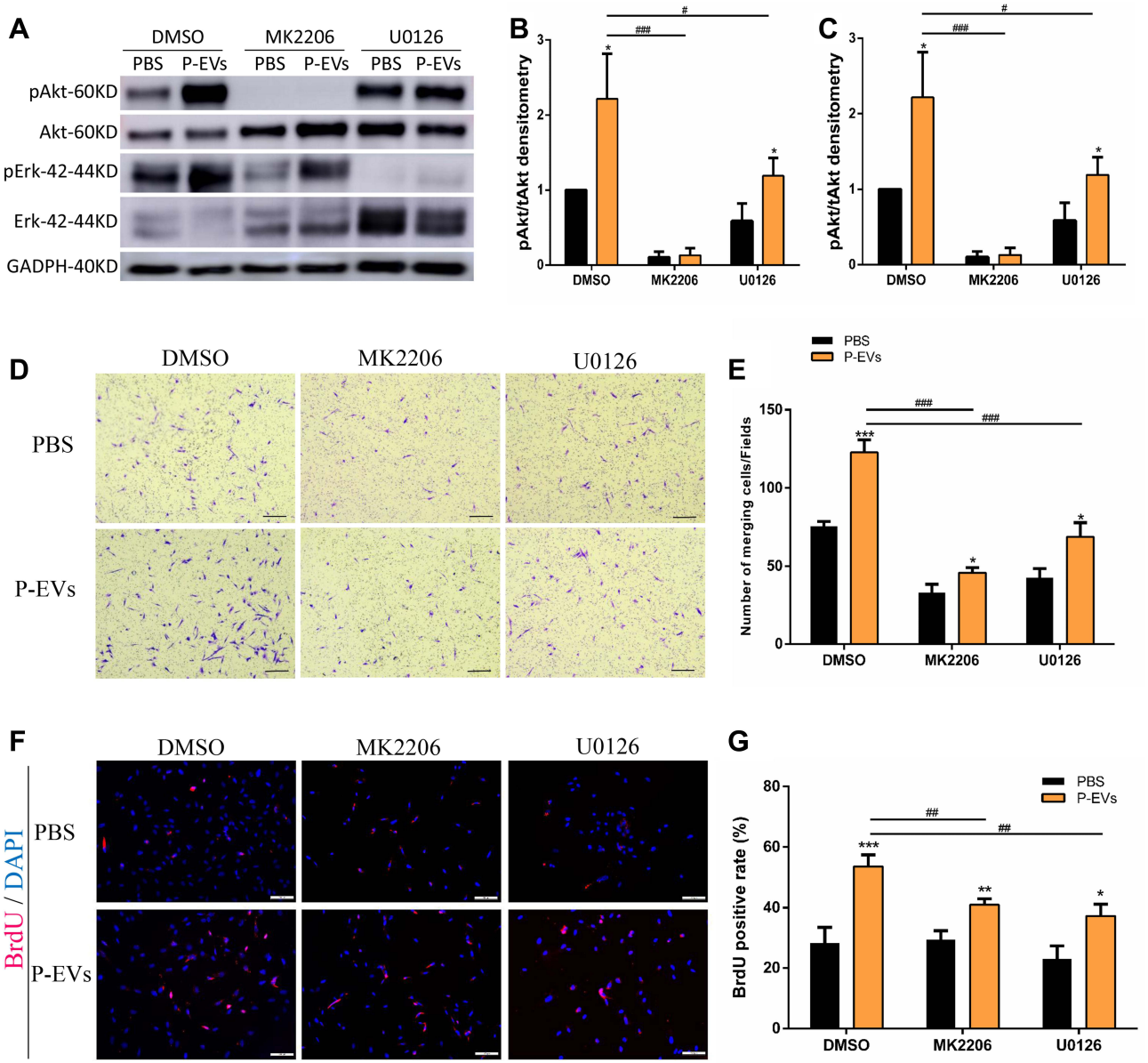

Figure 8 Periodontal ligament stem cell-derived small extracellular vesicle (P-EV)-mediated activation of Akt and Erk1/2 signaling and their effects on BMMSC migration. (**A**–**C**) Western blotting results showed that pretreatment with Akt inhibitor (MK2206, 10 μM) and Erk1/2 inhibitor (U0126, 10 μM) suppressed P-EV-induced Akt and Erk1/2 activation. *P <0.05 compared to phosphate-buffered saline (PBS) treatment, $^{\#}P$ <0.05 and $^{\#\#\#}P < 0.001$ compared to P-EV treatment. (**D**–**E**) AKT and ERK1/2 inhibition suppressed P-EV-induced cell migration. (**D**) scale bar = 100 μm. *$P < 0.05$ and ***$P < 0.001$ compared to PBS treatment, $^{\#\#\#}P < 0.001$ compared to P-EV treatment. (**F** and **G**) BrdU immunofluorescence assay showed that AKT and ERK1/2 inhibition suppressed P-EV-induced cell proliferation. (**F**) scale bar = 100 μm. *$P < 0.05$, **$P < 0.01$ and ***$P < 0.001$ compared to PBS treatment. $^{\#\#}P < 0.01$ compared to P-EV treatment. Representative results from independent experiments are expressed as the mean ± standard deviation.

Abbreviation: DMSO, dimethyl sulfoxide.

$P < 0.01$, respectively). These results suggest that P-EV-mediated AKT and ERK1/2 phosphorylation are partly facilitated through the adenosine receptor signaling pathway.

We further investigated whether AKT and ERK1/2 signaling are involved in the P-EV-induced migration of BMMSCs. Pretreatment with the AKT inhibitor MK2206 significantly blocked P-EV-induced phosphorylation of AKT ($P < 0.001$), and pretreatment with the ERK1/2 inhibitor U0126 significantly abrogated P-EV-induced ERK1/2 phosphorylation ($P < 0.001$) (Figure 8A–C). The results of migration assay at 24 h show that the P-EV treatment significantly promoted BMMSC migration compared with the DMSO control ($P < 0.001$). Quantitatively, AKT and ERK1/2 inhibition suppressed P-EV-induced cell migration by 2.69-fold ($P < 0.001$) and 1.79-fold ($P < 0.001$), respectively (Figure 8D and E). The BrdU immunofluorescence assay at 12 h showed that the specific inhibitor of AKT and ERK1/2 significantly suppressed P-EV-induced cell proliferation (Figure 8F and G).

To summarize these results, P-EVs immobilized in Matrigel and locally transplanted in a rat bilateral calvarial defect model accelerated bone tissue repair by increasing cell infiltration. Using BMMSC cultures, P-EVs were demonstrated to enhance cell proliferation and migration via activated phosphorylation of AKT and ERK1/2 in an adenosine receptor-dependent manner.

Discussion

Bone tissue engineering is associated with interdisciplinary factors, including seed cells, scaffolds, and biochemical/physicochemical factors. Despite the significant promise of MSC therapy for bone repair, an increasing number of studies have indicated that the paracrine action of MSCs could be utilized as a cell-free strategy.[5,7–10,19,22,24,25] As natural biocarriers of MSC paracrine secretions, sEVs are considered promising agents for bone regeneration.[4] However, the drawbacks of MSCs, including the donor age and the limited proliferative capacity, might hinder the quantity and quality of MSC-sEVs.[26] PDLSCs have been considered a suitable and abundant cell source for bone regeneration because of their easy accessibility and enhanced proliferation.[12,13] As periodontal ligament cells could increase mineralized matrix formation of bone marrow cells indirectly, PDLSC-derived secretome and sEVs are thought to have a pronounced influence on bone regeneration.[3,14,22,27] P-EVs participate in bone remodeling in mechanical environments via maintaining periodontal immune homeostasis.[28] PDLSC-derived conditioned medium could promote alveolar bone regeneration, which was at least partially attributed to sEVs.[27] The use of sEVs as biomimetic tools in bone tissue regeneration has recently gained attention.[29] To the best of our knowledge, our study is the first to use PDLSC-derived sEVs for calvarial bone repair in vivo.

To establish a local delivery strategy, P-EVs immobilized in Matrigel were transplanted into a rat model with bilateral calvarial defects. Matrigel was extracted from Engelbreth–Holm–Swarm mouse sarcoma for reconstituted scaffold preparation.[30] Being relatively radiolucent and resorbable when compared with bone substitutes, Matrigel has been widely used for space maintenance and loading biological factors in the calvarial defect model.[1] In the present study, Matrigel could deliver P-EVs to the injured bone tissues. With 3D spatial distribution in Matrigel, the encapsulated P-EVs enhanced bone repair when compared with the control side (without P-EV) in vivo, as analyzed via imaging and histological analyses. P-EV-induced bone repair was accompanied by the active proliferation of cells, as evidenced by the increased number of PCNA-positive cells in the defective site. Thereafter, we hypothesized that P-EVs immobilized in a 3D scaffold could promote bone repair by inducing the migration of host reparative cells, such as BMMSCs, to injured sites.

The effects of P-EVs on the cellular activities of BMMSCs were evaluated in vitro. Consistent with this hypothesis, the process of P-EV uptake by BMMSCs was confirmed, and P-EV treatment was observed to increase BMMSC migration and proliferation. According to a previous study, sEV uptake is dose-dependent and occurs via the caveolar endocytic pathway.[31] In the present study, the uptake assay was performed using 10 μg/mL P-EVs, and confocal microscopy analysis showed that the process of P-EV endocytosis by BMMSCs was time-dependent and saturable. The effect of P-EVs on the cellular activities of BMMSCs was consistent with previous studies, which showed that MSC-derived sEVs work rapidly to restore homeostasis and initiate the processes of endogenous tissue repair.[7,9] These observations suggest that P-EVs enhance bone repair through a synergistic effect on cell recruitment and growth.

MSC-derived sEV-induced tissue repair was consistent with the activation of pro-survival pathways, such as AKT, ERK1/2, and signal transducer and activator of transcription 3 signaling.[29,32–34] In the present study, P-EV treatment resulted in a prominent increase in phosphorylated AKT and ERK1/2 levels, indicating that the endocytosed P-EVs triggered the activation of AKT and ERK1/2 signaling pathways. The sEV-mediated regulation of cellular activities such as cell proliferation and migration has been partially attributed to the activation of AKT, ERK1/2, and p38 MAPK pathways.[29,35,36] This hypothesis was supported by our observations that the attenuation of protein phosphorylation with AKT and ERK1/2 inhibitors significantly inhibited P-EV-induced BMMSC migration, as analyzed through the transwell assay. It is noteworthy that AKT inhibition resulted in much greater attenuation of cell migration than ERK1/2 inhibition, suggesting that AKT might be a more important target of P-EVs than ERK1/2.

To investigate the upstream mediator of AKT and ERK1/2 signaling, the role of adenosine receptors was evaluated. Adenosine receptors participate in bone homeostasis by regulating both osteoclast and osteoblast function.[37] Theophylline, an adenosine receptor antagonist, attenuated both P-EV-induced AKT and ERK1/2 phosphorylation. P-EVs induced AKT and ERK1/2 signaling through the adenosine receptor pathway, which might be elicited by the PDLSC surface marker, CD73. Recent studies also suggested that sEV-carried CD73 functioned as a key enzyme to hydrolyze extracellular AMP to adenosine, which further enhanced adenosine receptor-mediated phosphorylation of AKT and MAPK.[8,16] CD73 is not only abundant and enzymatically active in MSC-derived sEVs, but has also been recently identified as a key bioactive component promoting sEV-driven rapid wound healing.[38–40] Notably, P-EV-induced phosphorylation of AKT and ERK1/2 in BMMSCs was significantly, but not completely, abrogated by non-selective blockade of adenosine receptors, which indicated that P-EV cargoes other than CD73 participated in P-EV-induced AKT and ERK1/2 phosphorylation. The cargo of MSC-derived sEVs is acquired from the parent cells and is highly complex and contains certain proteins and microRNAs.[8,37,41] Therefore, in the future studies, we will focus on the molecular contents of P-EVs to understand the role of CD73-mediated adenosine signaling in the activation of AKT and ERK1/2 signaling pathways.

The current study is merely a proof-of-concept study for the cell-free therapeutic strategy of P-EVs; however, some limitations should be addressed. First, the age of cell donors might be a reason for these encouraging results of P-EVs, since the pluripotential capacity and regenerative potential of PDLSCs decreased as age increased.[42] The age-related changes of P-EVs should be taken into account in further study. Second, P-EVs were gradually internalized by BMMSCs in vitro; nevertheless, the integration of P-EVs from the implantation site to the remote tissues over time needs to be explored in the future. Finally, in vivo results showed that P-EVs could induce significantly more bone formation than the PBS control groups but failed to close the defect completely. The bioactive scaffolds with a capacity of sustained release of MSC-derived sEVs might be a promising bone repair strategy.[43] In our previous study, a silk/laponite scaffold was developed with micron-scale porosities (1.3–4.5 μm), which might provide high specific surface area to carry P-EVs.[44] Therefore, the bioactive scaffold will be used for P-EV incorporation and release in the future.

Conclusion

In this study, P-EVs were immobilized in Matrigel and implanted on one side of the bilateral calvarial defects in a rat model. The effect of local transplantation of P-EVs was evaluated using the left and right self-controlled method. The results showed that the implanted P-EVs enhanced host cell proliferation and bone tissue repair in vivo. Using BMMSC cultures in vitro, cell migration and proliferation were enhanced by P-EVs treatment, and this effect could be partially attributed to the adenosine receptor-mediated activation of AKT and ERK1/2 signaling. Thus, this study provides a promising cell-free therapeutic strategy for bone repair that combines topical EV-implantation and extracellular matrix scaffolds.

Abbreviations

sEVs, small extracellular vesicles; P-EVs, periodontal ligament stem cell-derived small extracellular vesicles; PDLSCs, periodontal ligament stem cells; BMMSCs, bone marrow mesenchymal stem cells.

Acknowledgments

This work was surpported by the National Natural Science Foundation of China (No. 81701011) and the Youth program of Shanghai Municipal Health and Family Planning Commission (No. 20184Y0228).

We thank the Center of Cryo-Electron Microscopy (CCEM), East China University of Science and Technology, for the technical assistance on confocal laser scanning microscopy.

Disclosure

The authors report no conflicts of interest in this work.

References

1. Hsieh MK, Wu CJ, Chen CC, et al. BMP-2 gene transfection of bone marrow stromal cells to induce osteoblastic differentiation in a rat calvarial defect model. *Mater Sci Eng C Mater Biol Appl*. 2018;91:806–816. doi:10.1016/j.msec.2018.06.004
2. Spees JL, Lee RH, Gregory CA. Mechanisms of mesenchymal stem/stromal cell function. *Stem Cell Res Ther*. 2016;7(1):125–136. doi:10.1186/s13287-016-0363-7
3. Yu N, Bronckers ALJJ, Oortgiesen DAW, et al. Periodontal cell implantation contributes to the regeneration of the periodontium in an indirect way. *Tissue Eng Part A*. 2015;21:166–173. doi:10.1089/ten.tea.2014.0151
4. Liu S, Liu D, Chen C, et al. MSC transplantation improves osteopenia via epigenetic regulation of notch signaling in lupus. *Cell Metab*. 2015;22:606–618. doi:10.1016/j.cmet.2015.08.018
5. Witwer KW, Van Balkom BWM, Bruno S, et al. Defining mesenchymal stromal cell (MSC) derived small extracellular vesicles for therapeutic applications. *J Extracell Vesicles*. 2019;8:1609206. doi:10.1080/20013078.2019.1609206
6. Ko KW, Park SY, Lee EH, et al. Integrated bioactive scaffold with polydeoxyribonucleotide and stem-cell-derived extracellular vesicles for kidney regeneration. *ACS Nano*. 2021;15:7575–7585. doi:10.1021/acsnano.1c01098
7. Azoidis I, Cox SC, Davies OG. The role of extracellular vesicles in biomineralisation: current perspective and application in regenerative medicine. *J Tissue Eng*. 2018;9:1544427758. doi:10.1177/2041731418810130
8. Xu J, Wang Y, Hsu C, et al. Human perivascular stem cell-derived extracellular vesicles mediate bone repair. *Elife*. 2019;8:e48191. doi:10.7554/eLife.48191
9. Chew J, Chuah SJ, Teo K, et al. Mesenchymal stem cell exosomes enhance periodontal ligament cell functions and promote periodontal regeneration. *Acta Biomater*. 2019;89:252–264. doi:10.1016/j.actbio.2019.03.021
10. Li W, Liu Y, Zhang P, et al. Tissue-engineered bone immobilized with human adipose stem cells-derived exosomes promotes bone regeneration. *Acs Appl Mater Inter*. 2018;10(6):5240–5254. doi:10.1021/acsami.7b17620
11. Seo BM, Miura M, Gronthos S, et al. Investigation of multipotent postnatal stem cells from human periodontal ligament. *Lancet*. 2004;364(9429):149–155. doi:10.1016/S0140-6736(04)16627-0
12. Pan J, Deng J, Luo Y, et al. Thermosensitive hydrogel delivery of human periodontal stem cells overexpressing platelet-derived growth factor-BB enhances alveolar bone defect repair. *Stem Cells Dev*. 2019;28:1620–1631. doi:10.1089/scd.2019.0184
13. Zhang Y, Wang P, Wang Y, et al. Gold nanoparticles promote the bone regeneration of periodontal ligament stem cell sheets through activation of autophagy. *Int J Nanomedicine*. 2021;16:61–73. doi:10.2147/IJN.S282246
14. Nagata M, Iwasaki K, Akazawa K, et al. Conditioned medium from periodontal ligament stem cells enhances periodontal regeneration. *Tissue Eng Part A*. 2017;23(9–10):367–377. doi:10.1089/ten.tea.2016.0274
15. Chen L, Qu J, Mei Q, et al. Small extracellular vesicles from menstrual blood-derived mesenchymal stem cells (MenSCs) as a novel therapeutic impetus in regenerative medicine. *Stem Cell Res Ther*. 2021;12(1):433. doi:10.1186/s13287-021-02511-6
16. Wang X, Thomsen P. Mesenchymal stem cell-derived small extracellular vesicles and bone regeneration. *Basic Clin Pharmacol Toxicol*. 2021;128:18–36. doi:10.1111/bcpt.13478
17. Lin C, Kuo P, Chin Y, et al. Dental pulp stem cell transplantation with 2,3,5,4′-tetrahydroxystilbene-2-O-β-D-glucoside accelerates alveolar bone regeneration in rats. *J Endod*. 2019;45:435–441. doi:10.1016/j.joen.2018.12.019
18. Jiang X, Li X, Fei X, et al. Endometrial membrane organoids from human embryonic stem cell combined with the 3D Matrigel for endometrium regeneration in Asherman Syndrome. *Bioact Mater*. 2021;6(11):3935–3946. doi:10.1016/j.bioactmat.2021.04.006
19. Zhao B, Liu Y. Simvastatin induces the osteogenic differentiation of human periodontal ligament stem cells. *Fund Clin Pharmacol*. 2014;28(5):583–592. doi:10.1111/fcp.12050
20. Deng J, Pan J, Han X, et al. PDGFBB-modified stem cells from apical papilla and thermosensitive hydrogel scaffolds induced bone regeneration. *Chem Biol Interact*. 2020;316:108931. doi:10.1016/j.cbi.2019.108931
21. Théry C, Witwer KW, Aikawa E, et al. Minimal information for studies of extracellular vesicles 2018 (MISEV2018): a position statement of the International Society for Extracellular Vesicles and update of the MISEV2014 guidelines. *J Extracell Vesicles*. 2018;7:1535750. doi:10.1080/20013078.2018.1535750
22. Zhang S, Chuah SJ, Lai RC, et al. MSC exosomes mediate cartilage repair by enhancing proliferation, attenuating apoptosis and modulating immune reactivity. *Biomaterials*. 2018;156:16–27. doi:10.1016/j.biomaterials.2017.11.028
23. Zhang X, Kang X, Jin L, et al. Stimulation of wound healing using bioinspired hydrogels with basic fibroblast growth factor (bFGF). *Int J Nanomedicine*. 2018;13:3897–3906. doi:10.2147/IJN.S168998
24. Diomede F, D'aurora M, Gugliandolo A, et al. Biofunctionalized Scaffold in bone tissue repair. *Int J Mol Sci*. 2018;19(4):1022. doi:10.3390/ijms19041022
25. Pizzicannella J, Diomede F, Gugliandolo A, et al. 3D printing PLA/Gingival Stem Cells/EVs upregulate miR-2861 and −210 during osteoangiogenesis commitment. *Int J Mol Sci*. 2019;20(13):3256. doi:10.3390/ijms20133256

26. Sun Y, Zhang W, Li X. Induced pluripotent stem cell-derived mesenchymal stem cells deliver exogenous miR-105-5p via small extracellular vesicles to rejuvenate senescent nucleus pulposus cells and attenuate intervertebral disc degeneration. *Stem Cell Res Ther*. 2021;12(1):286. doi:10.1186/s13287-021-02362-1
27. Xu XY, Tian BM, Xia Y, et al. Exosomes derived from P2X7 receptor gene-modified cells rescue inflammation-compromised periodontal ligament stem cells from dysfunction. *Stem Cell Transl Med*. 2020;9:1414–1430. doi:10.1002/sctm.19-0418
28. Wang Z, Maruyama K, Sakisaka Y, et al. Cyclic stretch force induces periodontal ligament cells to secrete exosomes that suppress IL-1β production through the inhibition of the NF-κB signaling pathway in macrophages. *Front Immunol*. 2019;10:1310–1322. doi:10.3389/fimmu.2019.01310
29. Liang B, Liang J, Ding J, et al. Dimethyloxaloylglycine-stimulated human bone marrow mesenchymal stem cell-derived exosomes enhance bone regeneration through angiogenesis by targeting the AKT/mTOR pathway. *Stem Cell Res Ther*. 2019;10:335–349. doi:10.1186/s13287-019-1410-y
30. Trujillo S, Gonzalez-Garcia C, Rico P, et al. Engineered 3D hydrogels with full-length fibronectin that sequester and present growth factors. *Biomaterials*. 2020;252:120104. doi:10.1016/j.biomaterials.2020.120104
31. Huang C, Narayanan R, Alapati S, et al. Exosomes as biomimetic tools for stem cell differentiation: applications in dental pulp tissue regeneration. *Biomaterials*. 2016;111:103–115. doi:10.1016/j.biomaterials.2016.09.029
32. Zhang J, Liu X, Li H, et al. Exosomes/tricalcium phosphate combination scaffolds enhance bone regeneration by activating the PI3K/Akt signaling pathway. *Stem Cell Res Ther*. 2016;7:136–150. doi:10.1186/s13287-016-0391-3
33. Zhang S, Teo K, Chuah SJ, et al. MSC exosomes alleviate temporomandibular joint osteoarthritis by attenuating inflammation and restoring matrix homeostasis. *Biomaterials*. 2019;200:35–47. doi:10.1016/j.biomaterials.2019.02.006
34. Shabbir A, Cox A, Rodriguez-Menocal L, et al. Mesenchymal stem cell exosomes induce proliferation and migration of normal and chronic wound fibroblasts, and enhance angiogenesis in vitro. *Stem Cells Dev*. 2015;24(14):1635–1647. doi:10.1089/scd.2014.0316
35. Xu R, Zhang F, Chai R, et al. Exosomes derived from pro-inflammatory bone marrow-derived mesenchymal stem cells reduce inflammation and myocardial injury via mediating macrophage polarization. *J Cell Mol Med*. 2019;23:7617–7631. doi:10.1111/jcmm.14635
36. Zonneveld MI, van Herwijnen MJC, Fernandez-Gutierrez MM, et al. Human milk extracellular vesicles target nodes in interconnected signalling pathways that enhance oral epithelial barrier function and dampen immune responses. *J Extracell Vesicles*. 2021;10(5):e12071. doi:10.1002/jev2.12071
37. Mediero A, Wilder T, Shah L, et al. Adenosine A2A receptor (A2AR) stimulation modulates expression of semaphorins 4D and 3A, regulators of bone homeostasis. *FASEB J*. 2018;32(7):3487–3501. doi:10.1096/fj.201700217R
38. Hettich BF, Ben-Yehuda GM, Werner S, et al. Exosomes for wound healing: purification optimization and identification of bioactive components. *Adv Sci (Weinh)*. 2020;7:2002596. doi:10.1002/advs.202002596
39. Wada N, Maeda H, Hasegawa D, et al. Semaphorin 3A induces mesenchymal-stem-like properties in human periodontal ligament cells. *Stem Cells Dev*. 2014;23:2225–2236. doi:10.1089/scd.2013.0405
40. Angioni R, Liboni C, Herkenne S, et al. CD73+ extracellular vesicles inhibit angiogenesis through adenosine A2B receptor signalling. *J Extracell Vesicles*. 2020;9:1757900. doi:10.1080/20013078.2020.1757900
41. Henriques-Antunes H, Cardoso R, Zonari A, et al. The kinetics of small extracellular vesicle delivery impacts skin tissue regeneration. *ACS Nano*. 2019;13:8694–8707. doi:10.1021/acsnano.9b00376
42. Zhang J, An Y, Gao LN, et al. The effect of aging on the pluripotential capacity and regenerative potential of human periodontal ligament stem cells. *Biomaterials*. 2012;33:6974–6986. doi:10.1016/j.biomaterials.2012.06.032
43. Liu A, Lin D, Zhao H, et al. Optimized BMSC-derived osteoinductive exosomes immobilized in hierarchical scaffold via lyophilization for bone repair through Bmpr2/Acvr2b competitive receptor-activated Smad pathway. *Biomaterials*. 2021;272:120718. doi:10.1016/j.biomaterials.2021.120718
44. Wu M, Han Z, Liu W, et al. Silk-based hybrid microfibrous mats as guided bone regeneration membranes. *J Mater Chem B*. 2021;9:2025–2032. doi:10.1039/D0TB02687E